

University of Nevada, Reno

Improving the Photocatalytic Hydrogen Yield of $\text{Bi}_2\text{Ti}_2\text{O}_7$ via Fe Substitution

A thesis submitted in partial fulfillment of the
requirements for the degree of Master of Science in
Physics

by

Bradley C. Allured

Dr. Timothy Darling/Thesis Advisor

December, 2014

© by Bradley C. Allured 2014
All Rights Reserved



The Graduate School

We recommend that the thesis
prepared under our supervision by

BRADLEY C. ALLURED

Entitled

Improving the Photocatalytic Hydrogen Yield of $\text{Bi}_2\text{Ti}_2\text{O}_7$ via Fe Substitution

be accepted in partial fulfillment of the
requirements for the degree of

MASTER OF SCIENCE

Timothy W. Darling, Ph.D, Advisor

Vaidyanathan (Ravi) Subramanian, Ph.D, Committee Member

Paul Neill, Ph.D, Committee Member

W. Patrick Arnott, Ph.D, Committee Member

Benjamin T. King, Ph.D, Graduate School Representative

David W. Zeh, Ph.D, Dean, Graduate School

December, 2014

Abstract

$\text{Bi}_2\text{Ti}_2\text{O}_7$ (BTO) has been shown to be an effective material for photocatalytic hydrogen production, but is further improved by the low-level inclusion of Fe ions. This improvement is likely due to the introduction of interband electronic states, allowing for a multi-photon process in which electrons can be promoted to the conduction band by multiple photons of lower energy than is necessary in the single photon process in pure BTO.

The suspected mechanisms for the band structure alterations and hydrogen generation are presented. A method was developed for the synthesis of BTO nanoparticles, and allowing for the inclusion of Fe ions, and the material was characterized to confirm its structure, composition and physical properties. Hydrogen generation experiments were conducted in a slurry reactor with water and methanol, illuminated by a Hg-vapor lamp; a model was used to confirm validity of the measurements; and ultimately, BTO with 1% Fe inclusion is shown superior in hydrogen generation over BTO and a standard benchmark, commercially produced TiO_2 .

A reduced version of much of the information contained in this work also appears in *Applied Catalysis B: Environmental*, vol. 144¹. As many key items appear in both papers such content is not individually cited.

I dedicate this work in memory of Robert T. Allured, a man filled with more love, humor, mischief and crazy wisdom than anyone else I've met. We all have a lot to learn from his life, I am sorry he didn't get to see this, and sad only for the people who weren't lucky enough to know him. He will be missed, never forgotten.

I would like to acknowledge and thank my family and colleagues, without whose support, this work would not have been possible. I would like to individually thank Dr. Ravi Subramanian, the PI for this research, for his guidance and the opportunity to work on the project, and Dr. Tim Darling for his mentorship and countless conversations over the course of the research and many revisions of this thesis.

Table of Contents

Abstract.....	i
Dedication.....	ii
Acknowledgements.....	iii
Introduction.....	1
Theory.....	5
Material Preparation.....	11
3.1 Synthesis.....	11
3.2 Characterization	13
3.3 Characterization Results.....	15
Experiment.....	20
4.1 Hydrogen experiment apparatus.....	20
4.2 Measurement	23
Model.....	28
5.1 Minor functions.....	30
5.2 Gas temperature calculator.....	31
5.3 Slurry property calculator.....	31
5.4 Bubble generator	32
5.5 Column height calculator	32
5.6 Master modeling function	33
5.7 Approximations.....	34
5.8 Model results.....	35
Results.....	39
6.1 Hydrogen Experiment Results	39
6.2 Discussion	42

Chapter 1

Introduction

In any energy economy, two things are required: an energy source or a fuel, and a means to use the fuel to fulfill our energy needs on demand. There are several schemes that meet these basic requirements, each with its strong and weak points. Ideally, we would use a scheme with a renewable fuel; a complete cycle where the byproducts of fuel consumption can be used as precursors for fuel production. Here, I present progress in the fuel renewal link to complete the cycle for one such fuel, hydrogen.

We currently rely heavily on hydrocarbons, which meet our energy requirements excellently, but ecological and supply concerns have motivated research into alternative options. “Green” energy schemes, PV (photovoltaic), for example, have gained popularity. While the green energy sources are technically finite, we tend to call them “free” and “renewable” sources, but their intermittent nature, and inability to be throttled to meet demand, necessitate a means of storage. Grid storage returns us to hydrocarbons, and batteries are expensive, often toxic, and have to be replaced. “Storage” in the form of hydrogen has also been considered.

As a fuel, hydrogen gas can be burned and stored similar to natural gas. The only byproduct of burning hydrogen in air is water vapor with a slight possibility to form nitrous oxides. Or more elegantly, the hydrogen can be catalytically oxidized in a fuel cell, producing electricity, some heat, and water. The use side of the requirement seems to be met. Supply is the primary aspect hindering a hydrogen economy. At first glance, it

seems that being the most abundant element in the universe, hydrogen would be easy to come by. The problem is that the hydrogen atoms on earth are bound in molecules, largely water and hydrocarbons; the extremely light free hydrogen gas escapes to space.

Currently, 95% of US hydrogen gas is produced by steam reforming natural gas. Theoretically, the methane in natural gas reacts endothermically with ~ 1000 °C steam in the presence of a catalyst to produce carbon monoxide and hydrogen. The carbon monoxide reacts again with steam to produce more hydrogen and the final byproduct, carbon dioxide. In reality, the final byproducts can include other gasses, including carbon monoxide, nitrous oxides, and sulfur compounds, and of course, this method takes us back to the hydrocarbon issue.

Nearly all of the remaining 5% of hydrogen gas is produced via electrolysis; using an electric current to separate and concentrate auto-dissociated ions in water and allow them to form hydrogen and oxygen gasses. The main attribute of this process is that it can be completed without any use of hydrocarbons, and in fact uses the fuel byproduct, water, as the fuel precursor, thus completing the renewable cycle. Electrolysis, though, is only lightly employed, typically reserved for applications which require ultra-purity. This is because the process is inefficient, requiring a relatively big overpotential to overcome thermodynamic effects and large amounts of energy to produce a useful volume of the gasses. To combat the efficiency issue, platinum alloy electrodes are often used. Salts and/or acids are added to the water to aid in current flow, but the additives have to be carefully selected and can be toxic or dangerous.

It has also been demonstrated feasible to photocatalytically split water to produce hydrogen gas. The photocatalyst has the same purpose as any other catalyst; to assist

processes by providing multi-step mechanisms or reducing activation energies. But the photocatalyst is a light sensitive material that employs photons to enable a process similar to a mix of photodissociation with 6.7eV UV photons² and electrolysis by providing reaction sites and multi-photon energy, reducing the energy requirements on any single photon. Photons of sufficient energy produce electron-hole pairs in the catalyst, and the water is split in a series of redox reactions. This process is much more effective with the addition of an organic sacrificial agent which introduces intermediate chemical states and prevents the recombination of hydrogen and oxygen. It is possible that toxic organic industrial waste that pollutes ground water could be used as the sacrificial agent.

This process has the potential of using sunlight as the energy source to complete the renewable energy cycle in a hydrogen economy, and at the same time, could reduce the environmental impact of industrial waste. Further, because this can be done at the small scale, without the need for complicated or dangerous equipment or chemicals, it presents the possibility of on-site fuel production, thus removing transport concerns.

As of yet, photocatalytic water splitting cannot compete with the yield of steam reforming, progress in that direction is being made. What follows is a description of one approach to improving the photocatalytic process, using a previously tested compound, $\text{Bi}_2\text{Ti}_2\text{O}_7$ (BTO). Here, the inclusion of iron ions within the BTO is shown to significantly increase the volume of hydrogen yielded in small scale experiments modeled after the original work.

Chapter 2 provides a detailed explanation of the mechanisms suspected to be responsible for the photocatalytic process and description of how iron can improve the activity via modification of the BTO band structure. The photocatalyst is discussed in

chapter 3; the synthesis method is provided, and the various characterization tests are described with the results of the characterization. Chapter 4 lays out the specifics of the experimental method, apparatus, and measurement scheme. The validity of the measurement scheme is then verified in chapter 5, where the measured data is compared to the output of a simple model. Finally chapter 6 provides the results of the experiment, showing that BTO is improved by inclusion of small amounts of iron, and conclusions are drawn based on the experiment and model, with suggestions of future tests warranted by this work.

Chapter 2

Theory

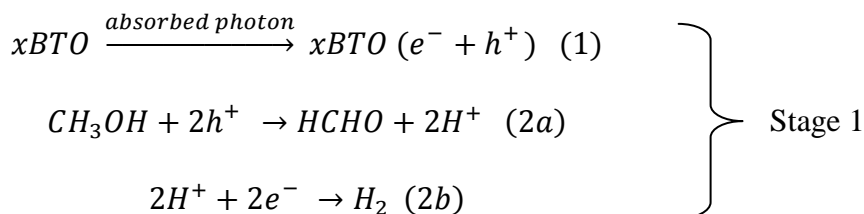
The process of dissociating hydrogen atoms (or dihydrogen molecules) from water or any other hydrogen-containing compound relies on being able to manipulate the electrons from the bonds in the compound to the bond in an H₂ molecule. Because the energy state of a compound is generally lower than the energy of its component parts, dissociation requires the addition of energy at least equal to the difference.

The dissociation energy for water, at 237.1 KJ·mol⁻¹, requires 2.46eV per molecule³, in a two photon process, this corresponds to 1.23eV or near infra-red photons. This suggests that the visible range of sunlight can be used to split water to produce hydrogen gas. Pure water splitting in this manner, however, does not occur because although separate ions form, they recombine almost instantly. A catalyst, called a photocatalyst due to its interaction with the exciting photons, can add more electronic states to the process and potentially provide a pathway for the separated ions to neutralize without recombining. The electronic structures of the compound and the catalyst interact and a photon may excite electrons in the catalyst to states that can be used in the dissociation.

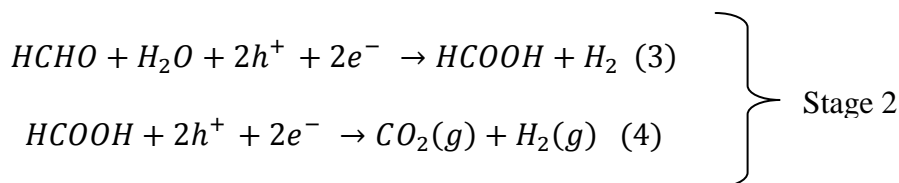
BTO acts as a semiconductor photocatalyst with a band gap close to useful (visible) wavelengths. The initial step in the process is the same as in a photovoltaic (PV) cell; an incident photon of sufficient energy promotes an electron into the conduction band, generating an electron-hole pair, or exciton. The aim is to make use of the exciton

in the dissociation reaction before it can recombine. In the case of a PV, the electron is separated in a circuit to create an electrical current. But in the case of the photocatalyst, the electron and hole, of sufficient energy, can each perform a reduction or oxidation reaction, respectively.

The water acts as an oxidant and a reductant, using both the electron and the hole^{3,4}. Through one possible pathway, requiring two excitons, an H⁺ ion is freed when water oxidizes, giving up an electron to fill a hole, the remaining OH oxidizes again, freeing a second H⁺. The two H⁺ ions are reduced to form H₂, and ½O₂ is left over. The produced ions recombine quickly to form water. While it is possible for H₂ and O₂ to form, without a means to separate them, they also tend to recombine to form water. The cyclic nature of the process means, again, almost no hydrogen is yielded.



Similarly,



Thus,

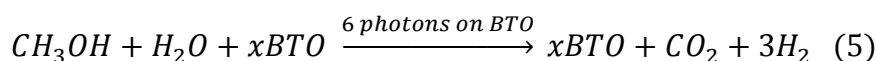


Figure 2.1 – Proposed chemical equations for the catalytic hydrogen generation process. It is split into two distinct stages, the second stage producing H₂ at a greater rate.

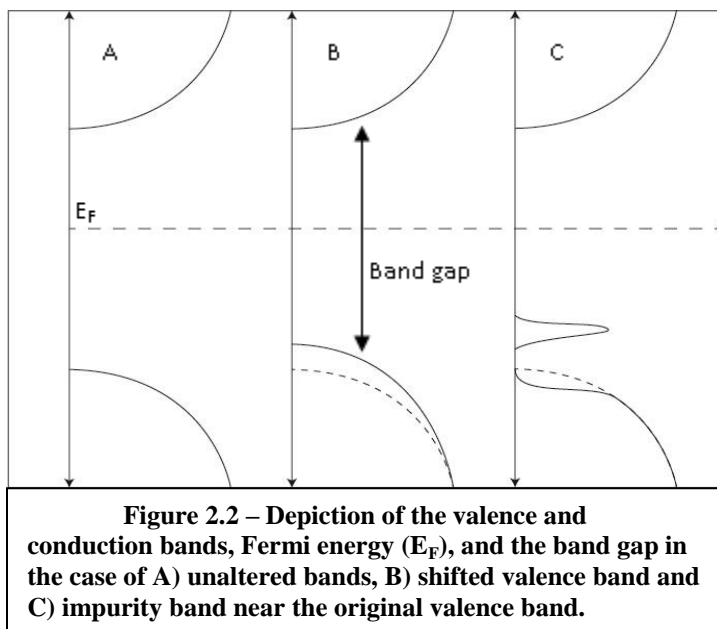
This is where the use of some sacrificial agent becomes important. In the case of this experiment, methanol (CH_3OH) was used to break the cycle by introducing intermediate chemical states, allowing all of the hydrogen to be harvested. While the water is a crucial component, and is indeed split in the process, it provides only 1/3 of the total hydrogen produced. The resulting redox reactions are shown in figure 2.1. The methanol is preferentially oxidized twice, with a dissociation energy of $64.1 \text{ KJ}\cdot\text{mol}^{-1}$ (corresponding to a 0.664eV , or short microwave/far infrared photon), to form two H^+ ions and a formaldehyde (HCHO) molecule^{5,6} (figure 2.1, eq. 2a). The formaldehyde is again oxidized, with yet a lower dissociation energy of $47.8 \text{ KJ}\cdot\text{mol}^{-1}$, next to a water molecule to form another two H^+ ions and a formic acid (HCOOH) molecule (figure 2.1, eq. 3). The formic acid has a negative dissociation energy of $-95.8 \text{ KJ}\cdot\text{mol}^{-1}$, which causes it to dissociate spontaneously on any hole site, producing two final H^+ ions and using two more holes to produce a single CO_2 molecule^{3,4} (figure 2.1, eq. 4). In each step, the two H^+ ions are reduced by the left over electrons to form one molecule of hydrogen gas (figure 2.1, eq. 2b). In short, six photons absorbed by the photocatalyst breaks down one methanol molecule and one water molecule, producing three hydrogen molecules and one carbon dioxide molecule (figure 2.1, eq. 5).

While the total process is described in three steps, it is considered to occur in two stages³. In the first stage, the methanol is decomposed to produce the formaldehyde with the hydrogen. With sufficient concentrations of formaldehyde, the second stage decomposes the formaldehyde and the formic acid readily decomposes. Partially due to the relatively lower and negative energy of the formaldehyde and formic acid reactions, respectively, as well as the greater abundance of water in the solution, stage two is

suspected to have a noticeably increased rate of hydrogen production than stage one. Consequently, a clear jump in detected hydrogen should be noticed when the methanol dominated stage one is over taken by the two-step dominated stage two³.

Recalling the energies required to overcome the reaction potentials, the water splitting was the highest, requiring two near IR photons. In fact, it is the only reaction whose photons need fall even close to the visible spectrum. Also recall that the exciton energy is based on the incident photon energy, which must meet the minimum requirement set by the catalyst material band gap⁷. Currently, one of the major limitations on the photocatalytic process is the material band structure. TiO₂, while promising in many ways (non-toxicity, catalytic activity, simplicity, etc.), is significantly limited by its absorbance, which lies almost entirely in the ultraviolet. It seems reasonable that the best solution is to use a photocatalyst that shares the desirable properties of TiO₂, but allows the band structure to be adjusted to our liking.

To this end, we consider the multi-metal oxides; BTO has been shown, theoretically⁸ and experimentally⁹, to exhibit a promising balance of the desired qualities. The interaction of electron states between the bismuth, titanium, and oxygen creates a plethora of orbital bands, allowing for a near continuum of photons to be absorbed in its absorption range, which naturally spans from blue deep into the UV. Already, BTO is capable of absorbing more of the solar spectrum we are looking for, but the unit cell of the crystal is much more complex, providing more sites for the substitution of other “impurity” or dopant ions to adjust the band gap.



There are two primary ways impurities can alter the band structure of a material: One, the interaction between the allowed energy states, or the band structure of the host material (the BTO in this case) and that of the dopant can cause a distortion of the band

structures, changing the band energies. Taking advantage of this phenomenon, the valence band can be pushed to higher energy, and/or the conduction band can be pushed to lower energy. Thus, the band gap is reduced directly. Two, the dopant can introduce one or more new bands that fall between the existing valence and conduction bands. Thus, the original bands are largely unchanged, but the intermediate impurity band can act as a new valence or conduction band or as a sort of stepping stone, making the effective band gap seem shorter.

There are many dopant candidates, but the inclusion of iron, mainly in the form of ferric oxide (Fe_2O_3) is well known, in small concentrations, to assist in photocatalytic processes. For this as well as for its abundance, stability, non-toxicity, and general ease of use, we focus on the Fe^{3+} ion. Further, as suggested by the electronic structure of iron, and hinted at by the black to reddish appearance of iron oxides, it seems a good candidate for decreasing the effective band gap of the BTO through the inclusion of impurity bands. While it is likely that the actual BTO bands are only slightly changed, the inclusion of

impurity bands allows a leap-frog effect where two photons can promote an electron to an impurity band and then a conduction band, sequentially, meaning lower energy photons are required. There, however, is likely a balance, as suggested by the small concentrations reported in literature; while the increased inclusion of iron in the crystal should continue to reduce the band gap, other factors, possibly the increase of “trap sites”, are likely to increase in the presence of increased iron inclusion. Different levels of iron inclusion within the BTO are investigated in an attempt to find an optimal balance.

Through characterization experiments, we can make preliminary suppositions of the effect of the iron inclusion. Through diffuse-reflection absorbance spectroscopy, we can see the influence the addition has on the absorbance spectrum of the BTO, and thus make generalized conclusions about the resulting change in the band structure. X-ray diffraction and electron microscopy allow comparison of the crystal structure and morphology, to ensure that the basic BTO is physically unchanged.

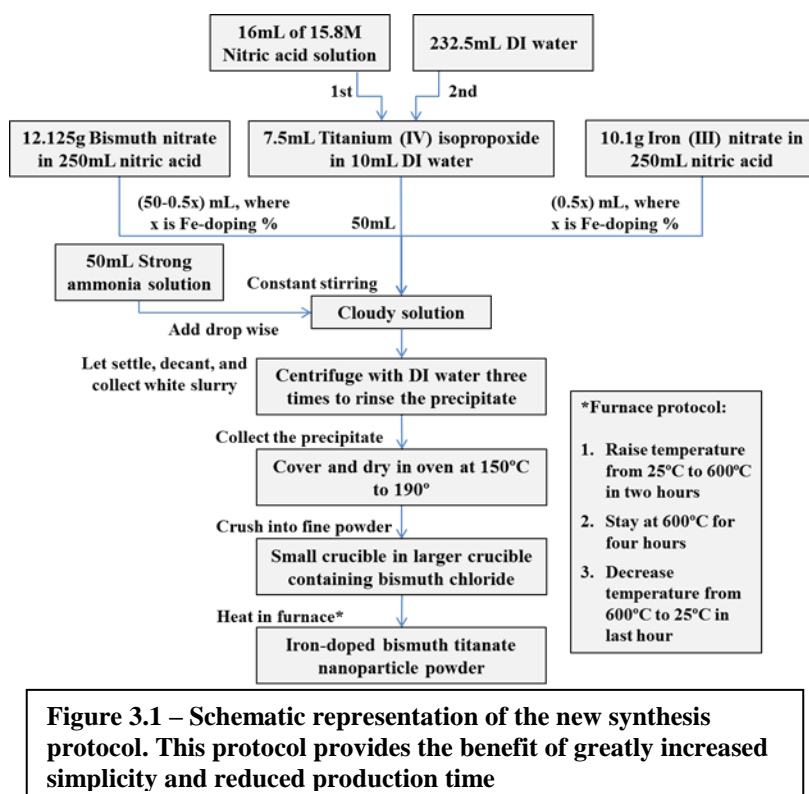
Chapter 3

Material Preparation

The preparation of the BTO falls into two main phases. The material is first synthesized, and then it is characterized. The following three sections discuss these two phases, with characterization divided into two sections: first the tests performed, and finally the results of the characterization tests.

3.1 Synthesis

The synthesis protocol is based on a previously reported method⁹, but is significantly different. The original method, described as “reverse micelle,” is based on a stoichiometric mixture of aqueous precursor solutions emulsified in isooctane with a surfactant. This synthesis method, shown in figure 3.1, has been shown to yield bismuth titanate ($\text{Bi}_2\text{Ti}_2\text{O}_7$) of the pyrochlore phase $((\text{Na}, \text{Ca})_2\text{Nb}_2(\text{O}, \text{OH}, \text{F})_7)$, a face-centered cubic structure ($\frac{4}{m} \bar{3} \frac{2}{m}$) in nanorod form. The down side to this method is that it is very sensitive to changes, and can be difficult to complete successfully; and even a successful sample takes about a week to produce. The synthesis protocol used in this experiment is entirely aqueous, easily repeatable, and can be completed in a single day.



To begin, the precursor solutions are prepared: bismuth nitrate and iron nitrate are dissolved to 0.1M, each in its own bottle, in 1M nitric acid. Titanium (IV) isopropoxide is hydrolyzed in water, dissolved in 16.8M nitric acid, and finally diluted to 0.1M in 1M

nitric acid. The titanium solution is unstable, and will form and precipitate TiO_2 within a couple of days, so the required amount of solution is prepared fresh on the day it is to be used – the other solutions can be stored for long periods. The solutions are then mixed in the desired stoichiometric ratio, with 50mL titanium, (50-0.5x) mL bismuth, and 0.5x mL iron solutions, where x is the desired iron-bismuth substitution percent.

Under constant stirring, 50mL of strong ammonia solution is slowly added (“squirtwise”) to raise the pH. As the pH increases, the ions of the three metals pick up excess OH ions and precipitate as hydroxide salts. After about ten minutes for settling, the supernate is decanted, and the remaining suspension is centrifuged, decanted, rinsed, and shaken multiple times to remove most of the ammonia. After many thorough rinses, the sample is centrifuged for extra time so that most of the water can be decanted, and the

thick, muddy consistency sample is placed in a beaker with a watch glass lid and placed in an oven long enough to finish drying it out. The resulting rocks are crushed to a fine powder and then calcinated in a furnace at 600°C for four hours in a configuration where a covered crucible contains bismuth oxide, and a smaller, open crucible containing the sample is nested inside, seated in the bismuth oxide. The presence of bismuth salts, either bismuth oxide or chloride, serves to increase the bismuth vapor pressure around the sample, which suppresses the bismuth in the sample from forming metallic bismuth and burning off. This protocol yields about 2g of BTO per batch.

3.2 Characterization

The first indicator of the success of synthesis is a simple visual observation. The product is compared to known good samples, for powder consistency and color. While this isn't a reliable, authoritative test, it serves as an indicator for how many and which tests need to be completed first.

Typically, the first characterization test is x-ray diffraction (XRD). Each sample was prepared on a glass slide, placing a small amount of powder on the slide and adding a few drops of acetone, leaving a very thin coating of the powder on the slide when the acetone dried. The pattern is compared to known BTO diffraction patterns for peak locations and relative intensities, and any extra peaks are identified. Additionally, a few samples were scanned a second time after use in a full run in the photocatalytic reactor to detect if the material had been altered by its use. Figure 3.2 shows some of these XRD scans.

The absorption spectrum of each sample was taken with a Shimadzu PC2500 UV-vis spectrophotometer between 300nm and 600nm. These measurements are made in diffuse reflectance mode, where the absorbance (A) is related to the transmitted (T) and reflected (R) intensities by $A=1-(T+R)$; $T=0$ in this case as the samples are opaque and backed by a reflective KBr substrate¹⁰. The samples were prepared by adding a small amount of powder to a mixture of ethylene glycol and citric acid¹¹, thinned with ethanol and thoroughly mixed in an apothecary to make a thick paste. The paste was then painted thinly onto a glass slide and slowly heated to 550 °C, burning off the organics, and leaving a film of the powder on the slide. While use of citric acid and ethylene glycol to form a nylon-like polymer, the Pechini method, has been reported in many other works¹²⁻¹⁴, the specific ratio of components and heating rate were a matter of trial and error.

The cutoff frequency can be determined from the data, which also allows calculation of the band gap energy. In figure 3.3, the rise of a new absorbance peak can be seen as a shoulder on the primary BTO peak, suggesting the formation of an impurity band with Fe inclusion.

Electron microscopy is typically a final characterization, reserved for only select samples (due to cost and time considerations). A scanning electron microscope (SEM) is used to examine the particle size and morphology. An energy-dispersive x-ray spectrometer (EDS) in the SEM also gives an approximate percent of each element composing the material. The crystallinity of the material is also examined with a high-resolution transmission electron microscope (HRTEM) and an included selected area electron diffractometer (SAED).

3.3 Characterization Results

X-ray diffraction (XRD) was performed as a first characterization step for each of the samples synthesized, and the spectra were compared to known spectra in the JCPDS catalog¹⁵. Each peak was identified, based on the known spectra, by its Bragg diffraction angle and relative intensity.

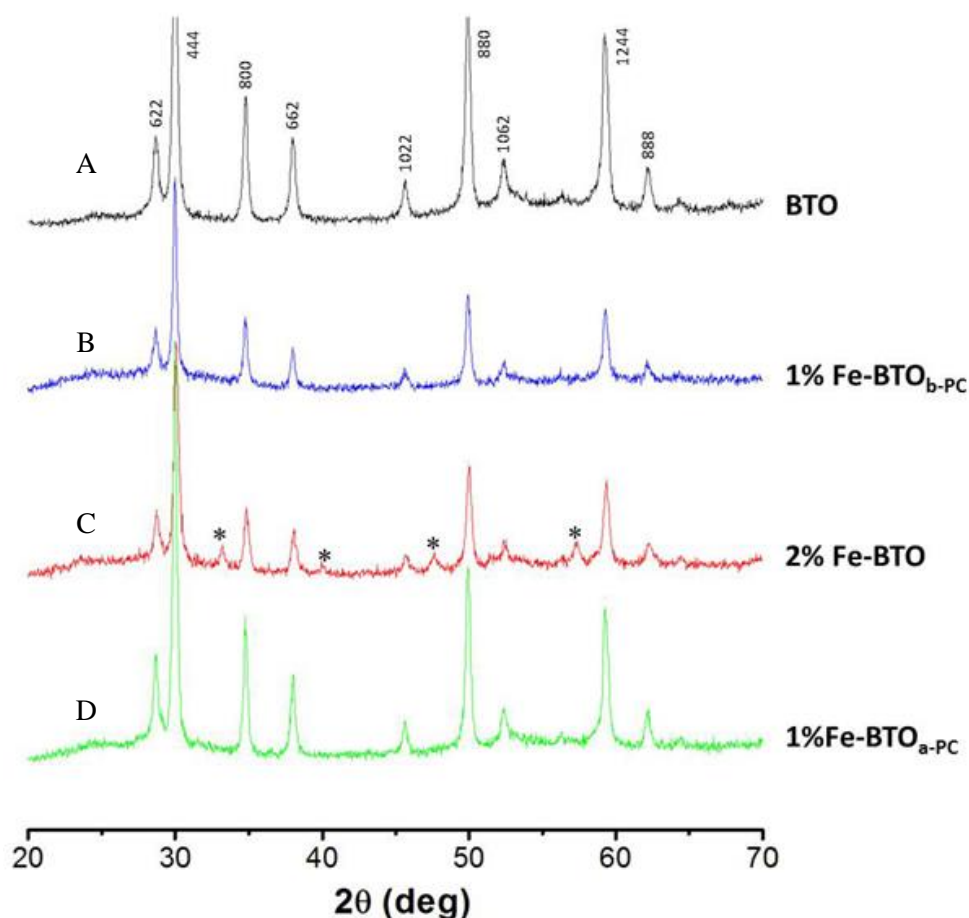


Figure 3.2 – XRD scans of various BTO samples (A) is the pure BTO with each peak labeled with its Miller indices. (B) is the initial scan of a 1% Fe-BTO sample, before photocatalytic reaction. (C) is 2% Fe-BTO, which shows four small extra peaks (marked by *), indicating the presence of Fe_2O_3 . And (D) is a scan of the same 1% Fe-BTO, post-reaction. Note the location and relative amplitude of the peaks appears the same for (A), (B) and (D).

The XRD spectra of pure BTO samples and samples at low Fe inclusion levels show the peaks, with the appropriate relative intensities unique to $\text{Bi}_2\text{Ti}_2\text{O}_7$ (JCPDS #32-

0118), with no evidence of other phases. XRD analysis was also performed on a few samples that had been used in the hydrogen generation reactor. Most of these samples had been exposed to the experimental condition for two hours, but one sample was exposed for about six hours and two samples were exposed twice for two hours each. In all cases, the XRD spectrum was unchanged by exposure to the conditions within the reactor, suggesting a strong reusability of the catalytic material.

In some samples, specifically those synthesized with a higher iron substitution, low level ferric oxide α -(Fe_2O_3) XRD patterns (JCPDS #89-8103) were observed. When compared to an equivalent mixture of BTO, and Fe_2O_3 to the intended substitution level, the Fe_2O_3 peaks were much lower magnitude in the synthesized sample, suggesting most of the iron added was incorporated into the BTO, and only a small portion formed Fe_2O_3 .

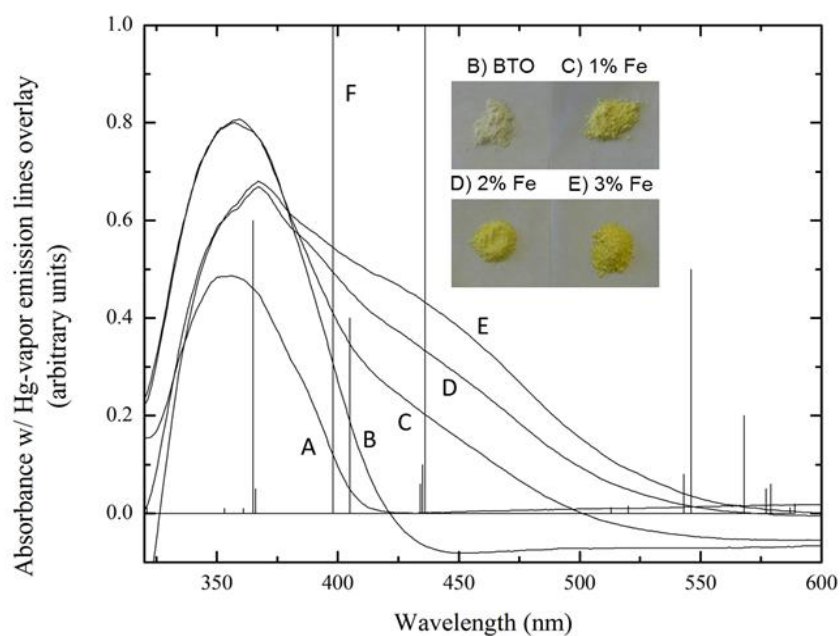
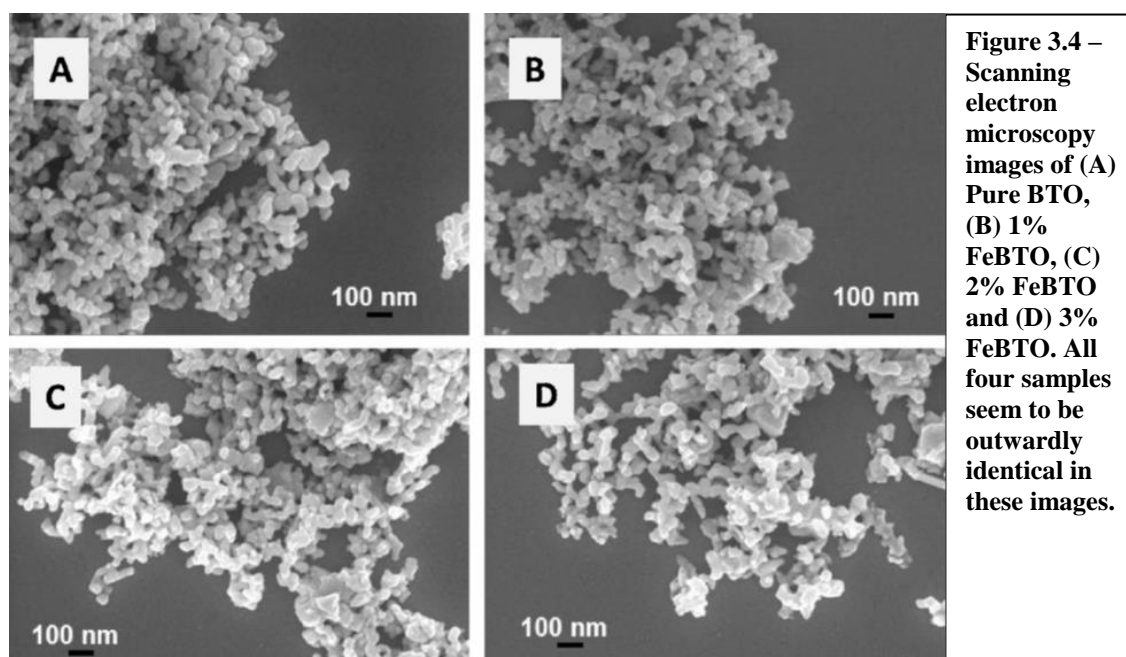


Figure 3.3 – Absorbance spectra of (A) TiO_2 (B) BTO, (C) 1% Fe-BTO, (D) 2% Fe-BTO, (E) 3% Fe-BTO and (F) mercury vapor emission lines overlaid for reference. The inset shows a darkening yellow color with increased Fe substitution as a result of the increased amplitude of the suspected impurity band absorption peak.

This observation is further corroborated by photon absorbance spectra collected between $\lambda=300$ nm and $\lambda=600$ nm for these samples. The spectra were qualitatively compared to both BTO and Fe_2O_3 absorbance spectra. The BTO signature seemed present and unchanged in all samples, except that a shoulder appeared on the longer wavelength side of the main peak, increasing in amplitude with Fe substitution percent. At lower substitution levels, the Fe_2O_3 signature was not detected, but at levels at and above 3% (and one sample at 2%) the Fe_2O_3 signature seemed to begin to show at the high λ end of the scans, indicating that the iron was incorporated into the BTO at lower substitution levels, but at the higher substitution levels, some of the iron formed Fe_2O_3 instead of being incorporated in the BTO.



Scanning electron microscopy (SEM) was performed in the University of Nevada Chemical and Material Engineering Department on unused samples of all substitution levels from 0% to 3%, shown in figure 3.4, as well as a pure BTO sample before the final calcination step in the synthesis procedure and a 1% FeBTO sample after two hours

exposure to the conditions within the experimental reactor. The unused samples showed a consistent morphology as clumps of nanoparticles with an average size of 50 ± 15 nm. Differing substitution levels showed no visible alteration to the structure of the particles; in size, grouping, shape, or overall outward appearance. The sample which had been exposed to the experiment also seemed essentially identical under SEM scrutiny. The uncalcinated sample, however, showed much larger particle size, greater than 80 nm, and a high level of variability in shape and size, suggesting the final state of the catalyst is largely dependent on the calcination step; this seems to be confirmed by both a previously published work which used a different protocol to produce nanorods⁹ and by XRD data on the uncalcinated samples, showing no evidence of the BTO crystalline structure. The synthesis procedure for the nanorods was attempted by multiple people in our lab, including myself, but none were successful; though the closest attempts yielded what seemed to be the appropriate precalcinated material and BTO, and it seems, again, the final calcination step is the key to the different morphology, nanorods were not successfully produced in any of these attempts.

The SEM hosted an EDS which was used to further characterize the samples. This equipment, however, proved to have its own set of complications. EDS data processing algorithms can easily confuse x-ray spectra by misidentifying individual peaks, and properly correcting such errors requires a specialized expertise that we do not have or have access to. Primarily, many of the EDS results displayed relatively rare elements that should not have any reason to have appeared; namely, gold and platinum were abundant in many of the scans. None of these elements were used in the synthesis or had even been used in the lab in any reasonable stretch of time, nor was any sign of them detected in any

other characterization test performed. Because of this, the EDS data must be taken for what it is: a qualitative indicator of the elements expected. While we had hoped EDS to reveal the true constitution of the material, it is believed this is not the case. There are many possible factors that could play into the situation: cross contamination, even from the SEM itself, could be a contributor, the intended use of the EDS could be another... EDS is often used to analyze ore samples, looking for precious minerals, and with the rich mining interest at the University of Nevada, it is not unreasonable to believe this piece of equipment is calibrated to identify those first. Nevertheless, the EDS does identify the expected elements in approximately the ratios expected.

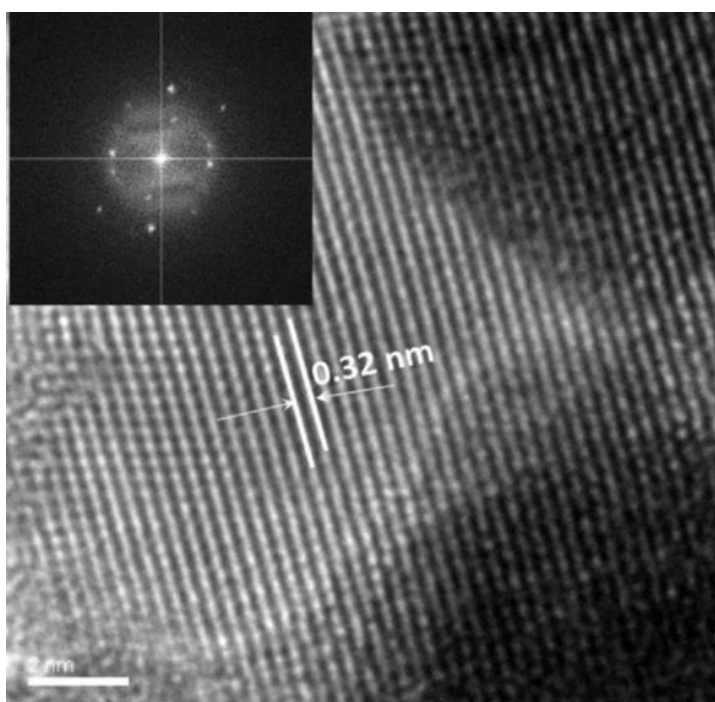


Figure 3.5 – High-resolution transmission microscopy (HRTEM) and (inset) selected area electron diffraction (SAED) of 1% FeBTO, showing crystallinity of the sample.

Finally, high-resolution transmission electron microscopy (HRTEM) was performed (also in the University of Nevada Chemical and Material Engineering Department) on a few samples (the number of samples was limited by cost and time). The HRTEM images show the sample is polycrystalline, and further, the 3.2 nm interplanar

spacing, shown in figure 3.5 is consistent with the 622 plane (corresponding to the first marked peak in figure 3.2) of the expected Pyrochlore BTO results.

Chapter 4

Experiment

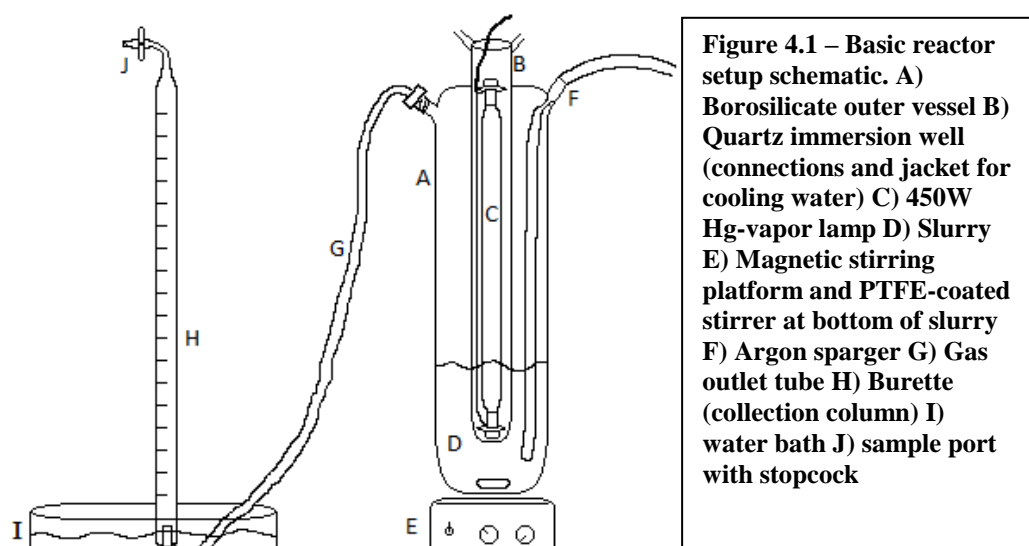
Because this work is meant to improve on results from previous work^{8,9}, the experiment was designed beginning with the original apparatus and methods. As work proceeded and opportunities were recognized, the experiment was modified to improve consistency and accuracy. Additional measurement points were also added to reveal more of the workings and environment within the reactor. The over-all feel of the experiment, however, was kept similar to the original work so that comparisons could be made.

4.1 Hydrogen experiment apparatus

The main component of this experiment is the reactor (from Ace glass¹⁶). It consists of a borosilicate outer vessel and a quartz, cooling water jacketed, immersion well which allows a 450W medium pressure mercury vapor lamp to be placed in the center of the reactor. The immersion well seals to the outer vessel via a ground glass joint. A magnetic stirrer continuously stirs the slurry in the outer vessel. Argon purging gas enters through a sparger tube which is polymer tubing from an argon bottle (regulated to 2PSI and flow controlled by a needle valve) to nearly the bottom of the vessel (below the surface of the slurry). The tubing is glued to a ground glass connection that seals to the vessel. The gas outlet tube is connected to the outer vessel via a bored nylon bolt, sealed with PTFE tape.

In an attempt to better control variables and improve measurements, some additional components were tried out. Check valves were placed in the argon and gas

outlet tubes to prevent backflow resulting from pressure changes. A gas sampling bulb was also added inline on the gas outlet, between the reactor and the water bath. These were ultimately removed in favor of simplicity because gas leaks became a serious issue. Additionally, many tests were run to replicate previous results from similar experiments with this reactor. Toward that end, the reactor was configured to match the previous experiment.



The gas expelled from the reactor travels down the gas outlet tube, and when the pressure becomes high enough to displace the water at the bottom, it bubbles into an inverted burette in a water bath. The gas collects at the tip of the burette, where it can be sampled through a luer stopcock. Figure 4.1 is a simplified sketch of the reactor setup.

The experiment initiation procedure is as follows: 0.150g of the powder to be tested is added to the clean reactor with the stirrer. Then, 250mL of deionized water and 50mL of methanol, creating 300mL of 5:1 water to methanol solution, is added, and the stirrer is switched on. The ground glass joints are sparingly greased and sealed, and the nylon bolt is wrapped in PTFE and secured, sealing the reactor. The water bath is filled

and the gas outlet tube is fed about 2cm up into the burette. Water is drawn into the burette via the sampling port until water fills the entire burette, and the stopcock is sealed. The cooling water is turned on to a specified position on the knob, and the argon is turned on so that it fills the burette and a few bubbles per second escape through the bottom of the burette. The reactor is left like this for about 30min in a blacked out, closed fume hood to allow the argon to flush the system and the temperatures to reach a steady state. Finally, the reactor can be started. The argon is stopped, the water is drawn back into the burette to the starting level (because the burette is inverted, the 50mL mark is zero, and as gas is collected, the water level will fall toward the 0mL mark), the lamp is switched on, and a timer is started.

The lamp takes about 2min to warm and reach steady operation. The reactor, however, continues to heat for much longer. From about 3min to about 10 or 12min, the reactor gas temperature increases so drastically, the resultant gas expansion and water evaporation causes a constant bubbling in the column. When the initial bubbling slows, the column is nearly filled with gas, so the water level is returned to the starting position (a sample is tested for hydrogen, but it is rarely detectible in this first sample). The reactor is run for 2 hours with gas samples removed and tested every 30min (this frequency is limited by the time required for each sample in the gas chromatograph). While the lamp is on, UV goggles are worn and the blacked out hood door is kept closed as much as possible for safety from the UV radiation and to keep the temperature as stable as possible.

After completing an experiment, the lamp is switched off, the reactor seal broken (to prevent vacuum pulling water into the reactor from the bath), and cooling water left on long enough to cool the glass to a temperature at which it can be handled safely. The slurry is either recovered for further testing or discarded. The outer vessel and stirrer is scrubbed with glassware detergent and rinsed with deionized water. The immersion well and sparger is carefully cleaned with ethanol and dried. Ethyl acetate can be used, with vigorous scrubbing, to remove excess grease, and acetone then ethanol is used to remove any residue.

4.2 Measurement

The main measurement for this experiment is taken with a gas chromatograph (GC) from SRI Instruments¹⁷ (not affiliated with SRI international, formerly Stanford Research Institute). The GC is an empirical instrument, its output data (mV vs. time graph) cannot be interpreted from first principles; rather, it must be calibrated by running known samples to create a calibration curve. To ensure accuracy, this was performed with many samples, each of which was repeated many times.

Basically, the way the GC works is a thin copper tube coil in an oven is packed with a ceramic analyte. A constant flow of ultra-pure argon (helium can also be used to detect heavier compounds) passes through the column as a carrier gas. At the beginning of a scan, the sample is injected through a septum at the front of the column. Due to surface interactions on the analyte, different compounds will travel through the column at different rates; this separates the constituents of the sample to be detected by a

thermocouple filament at different times. The oven also slowly heats the column to allow the “stickier” compounds to travel through the column at a reasonable rate. Finally, the thermocouple filament at the exhaust end of the column measures the heat transferred to the gas as it exits (argon is ignored as it is the carrier gas and is subtracted from the background). The result of this process is a graph of mV vs. time, where compounds appear as peaks at different times; the peaks are typically Gaussian, asymmetry of peaks is an indicator of a potential problem. The center of the peak for each compound is at about the same time on each run (the time can be affected by the timing between the run start and sample injection as well as how quickly the sample is injected), and the area of the peak corresponds to the amount of the compound detected.

Caution should be exercised when using this instrument as its data can mislead the user. Because of the nature of the instrument, unknown peaks can only be identified by sampling known gasses until one is found to create a similar peak; thus, assumptions about which compound each peak indicates (or that it is a single compound) could be false. Also, this GC is designed for the detection of non-polar hydrocarbons, which leads me to believe the analyte is incompatible with polar molecules like water – the documentation for the instrument is insufficient to determine the validity of this belief, but observation of the instrument’s behavior seems to support it. In all, there seems to be a considerable amount of opportunity to inadvertently misinterpret data through false assumptions or create meaningless data through careless operation. I have developed a procedure for running the GC so as to collect useful and relatively consistent data – the most important aspect is not necessarily the specific steps, but to consistently perform the same steps in the same order and at the same intervals every time. While minor changes

can affect the measurements, I have confirmed, through many repeated measurements of known and unknown samples, that careful consistency allows good repeatability. This convinces me that while I cannot be confident to more than about 10% in any single measurement, the confidence in any trends between subsequent measurements is much greater – to within about 1%.

While the reactor is being prepared, the GC is turned on and allowed to warm up. When it is ready, a blank run (no sample injection) and an automatic bake cycle are started simultaneously to clear the analyte of any residual gas and especially any water. After this step, the GC is ready to use (there is a cool-down period after every run).

Once the reactor is in operation and gas is being produced, there is a set of steps involved in taking each measurement. As mentioned above, the first sample is taken at about 10-12min, and the column is reset to its starting position. At all of the following sample times, the column is not reset unless it is absolutely necessary to make room for more gas production.

To take a sample measurement, the time and column volume (V) reading are recorded. A gas-tight, valved syringe is connected to the stopcock, and with the stopcock and syringe valve open, 1mL of gas is smoothly drawn off the top of the column, and both valves are closed before disconnecting the syringe. The collected sample is fed into the GC as follows: a fine needle is connected to the syringe and inserted through the septum, the syringe valve is opened, immediately following this, the sample is injected over about 1 second while the run start button is simultaneously pressed, and finally, the needle is immediately removed. At this point, any excess gas can be removed from the column to reset it, if necessary. The volume of gas removed and the integrated area of the

hydrogen peak from the GC are recorded. This process is completed as quickly as possible without introducing a risk of additional error.

The calibration of the GC is such that the concentration of hydrogen in the 1mL sample is calculated by dividing the integrated peak area by the calibration constant. The volume of hydrogen gas removed from the column is calculated by multiplying the concentration of the sample by the volume of gas removed at that sample time. A running sum is kept of removed hydrogen volume. The volume of hydrogen in the column is calculated similarly, multiplying the concentration by the gas volume in the cylinder, $50\text{mL} - V + 3.7\text{mL}$ (recall the starting point on the inverted burette is 50mL, and the readings decrease as gas is collected. Also, there is a 3.7mL head space in the burette). A running sum is also kept for the column hydrogen volume. Adding the two hydrogen volume sums at each sample interval produces the total hydrogen released from the reactor up to that point. The total hydrogen gas volume released at the end of the experiment is converted to a rate ($\text{mL}\cdot\text{hr}^{-1}$) which is then normalized by moles of catalyst ($\text{mL}\cdot\text{hr}^{-1}\cdot\text{mol}^{-1}$) for comparison with other catalysts, primarily TiO_2 (Degussa P25¹⁸).

A number of peripheral measurements were also taken to help form an understanding of the mechanics of the experiment and collect parameters for the model (discussed in chapter 5). Physical dimensions were measured with a scale and Vernier caliper. The bubbling was recorded on video to allow estimation of bubble rates and volumes. A monometer was used to measure the pressure the reactor reaches before bubbling as well as to observe the pressure changes during an experiment. An Exetech 4-channel data logger equipped with k-type thermocouples was used to take temperature measurements at 1Hz for the duration of experiments. Temperature data was collected in

the water bath and the water in the column, in the air inside the hood, and on the outer vessel glass at the bottom, just below the water line, just above the water line, near the top, and half-way between the previous two locations. Additionally, one of the probes was shielded with a 1/8" steel tube and sealed with RTV sealant, and was used to measure the temperature of the gas inside the reactor (both behind additional shielding from the lamp light and under direct illumination) and the slurry in the bottom.

Chapter 5

Model

The purpose of the model is to use a simplified “virtual reactor” in an attempt to replicate the results from the physical experiment. That is, this model is used to verify that all parts of the reactor, including the slurry and gases are behaving as expected, to show the validity of the measurement scheme, and to reveal aspects of the system which we were not able to physically measure. The model assumes (an adjustable) constant rate of H_2 production; it does not model any of the photon-catalyst interactions or the chemistry occurring within the reactor. Most of the calculations involved are based on fundamental concepts of thermodynamics, and to avoid a meaningless fit resulting from a function with too many free parameters, the model was kept as simple as possible. Initially, many assumptions were made (e.g. slurry temperature effects, dissolved gasses, and water

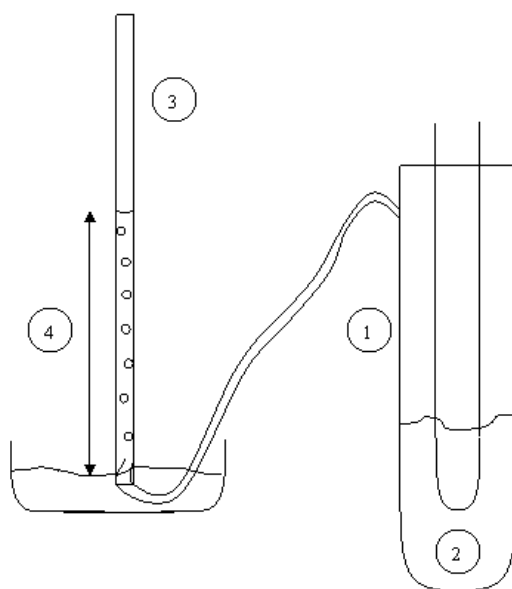


Figure 5.1 – Diagram of the physical reactor with four regions marked. The numbers shown correspond with the labeled functions in figure 5.2. The Master Modeling Function handles calculations and variables in all four regions. Region one is the gas within the reactor, or “reactor gas,” and two is the “slurry” in the reactor. Region three is the expelled gas collected in the “column,” and region four is the downward displaced column water.

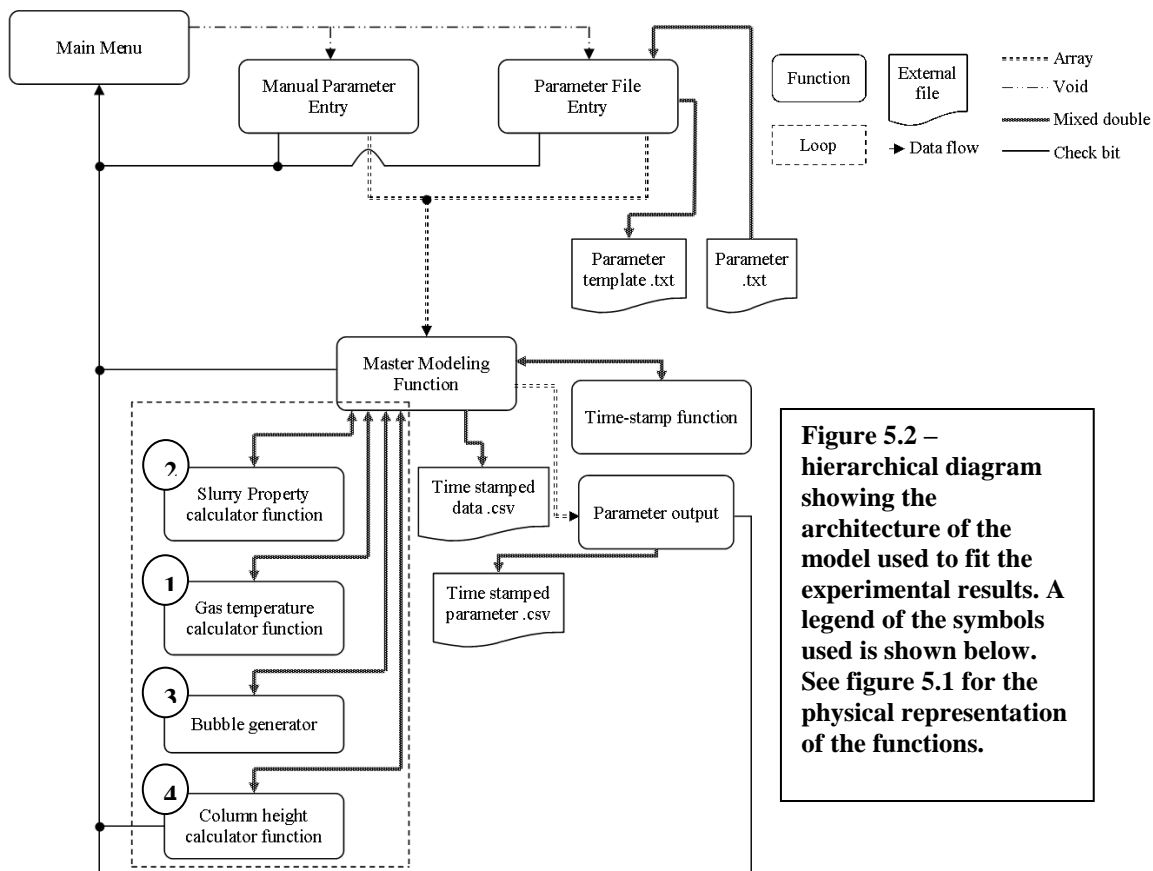


Figure 5.2 – hierarchical diagram showing the architecture of the model used to fit the experimental results. A legend of the symbols used is shown below. See figure 5.1 for the physical representation of the functions.

vapor were ignored, and all gasses were treated as ideal) to create a first approximation.

From the model output, and careful observations and measurements of the physical reactor under specific conditions, the model was improved by adding the lowest order perturbations, one at a time until a reasonable fit was reached. The added perturbations included functions that closely follow the temperature of the gas and slurry and calculate the pressure and amount of water vapor. Through this process, we can gain insight into the influence of individual pieces of the mechanics. Figure 5.1 shows the part of the physical reactor that each function handles, and figure 5.2 shows the basic architecture of the model program

The following sections describe the functions used and the results obtained from the model.

5.1 Minor functions

Because they do not serve much of a purpose in terms of scientific content, five minor functions will be briefly described here. The “Main Menu” function serves as an entry and safe exit point to the model. It is the hub, which allows the user to select how they wish to run the program. The “Manual Parameter Entry” will prompt the user to enter each of the parameters, one at a time, and create a parameter array (which is later output to a .csv file for reference) from the entries, while the “Parameter File Entry” function will create the parameter array from the data read from a specified .txt file. It can also be prompted to create a template file for reference. Both of these two functions will report any error before automatically aborting and have a manual abort option. Any kind of abort will return the user to Main Menu. After completing successfully, either function will send the parameter array to initialize the “Master Modeling” function. The “Time-stamp function” simply uses the system time to create a time-stamp with date and time and formats it to be used as a unique output file label. It takes no initialization values, and returns the time-stamp to the Master Modeling function. Finally, the “Parameter output” function is initialized with the parameter array and a time-stamped output file name, and writes a human readable .csv parameter file. The same time-stamp is used for this parameter file and the main data output file to make it easy to keep track of which initial parameters were used to create each dataset. The Parameter output file will report any errors before aborting to Main Menu if a file error occurs.

5.2 Gas temperature calculator

Initialization values: time. Return values: gas temperature. Ambient temperature is static at the average recorded value, 25.1°C. The gas temperature is kept at ambient temperature for the first 127s, after which it is calculated as a logistic function of time,

$$T = \frac{A_1 - A_2}{1 - (t/t_0)} + A_2, \text{ based on and fit to recorded temperature data.}$$

5.3 Slurry property calculator

This function handles calculations based on the temperature of the slurry in the reactor.

Initialization values: gas temperature, time, rate constant (C) and reaction energy (E_g)

from the rate equation $r = C e^{-E_g/kT}$ (K is the Boltzmann constant), reactor gas volume,

and the gas volume in the tubing connected to the reactor. Return values: reaction rate,

water vapor pressure, number of water vapor molecules in the reactor and tubing, and

slurry temperature. The slurry temperature is calculated the same way as the gas

temperature in section 5.2, but with different constants, also based on recorded

temperature data. Water vapor pressure is calculated as a function of temperature from

the Antoine equation¹⁹. The water vapor is then treated as an ideal gas, and the number of

vapor molecules is approximated from the ideal gas law with the vapor pressure, the

temperature and volume of the reactor gas, and the volume of the connected tubing at

ambient temperature. Finally, the reaction rate is calculated from the rate equation above.

5.4 Bubble generator

When the reactor reaches the critical pressure (the pressure exerted by the water in the section of tubing at the bottom of the water bath, under the column), this function generates a virtual bubble. Initialization values: pressure differential between the reactor gas and atmosphere, reactor gas temperature, reactor gas volume, and tubing gas volume. Return values: number of gas molecules expelled in bubble. The number of molecules expelled is calculated from the ideal gas law, such that it is the number of molecules required to cause the pressure differential in the reactor at its current time and the tubing at ambient temperature. The bubble is later split into its constituents to be passed from the reactor to the column; the Master Modeling Function handles this operation.

5.5 Column height calculator

The height of the water in the column is calculated here. Initialization values: column internal radius, initial water height, column head volume, atmospheric pressure, total number of gas molecules in the column. Return value: column water height. Because the water column will pull a slight vacuum on the gas above it, the gas pressure will not be at atmospheric levels, and changes based on the height of the water column. The calculation is based on the ideal gas law, but as the number of molecules changes, so does the water height (connected to volume), and hence the pressure of the gas. To account for the second unknown (pressure) in the equation, an equation describing the gas pressure as a function of water height is substituted into the equation. The resulting equation gives a quadratic, the two solutions of which are calculated using the quadratic formula. Logic tests then decide which solution is un-physical and which is right. The correct value is

then returned. If the solutions are imaginary or neither seems physical, an error is reported and the model is aborted.

5.6 Master modeling function

This function handles data compilation and output, the bulk of the calculations, and calls the supporting functions that handle the other special calculations. Initializing values: user-defined parameter array. There are no returned values. This function begins with housekeeping type tasks, initializing the data list and variables with initial conditions and creating a timestamp and the output files. It then enters a time loop to perform the experiment – inside the time loop is the virtual lamp switched on. First, the Gas temperature and Slurry property calculator functions are run, the amount of hydrogen in the reactor gas is calculated based on the calculated rate, and the total amount of gas (and the concentrations of gasses) is calculated. The reactor pressure is calculated and tested against the critical pressure. If the critical pressure is exceeded, the bubble subroutine is entered. In this sub routine, the Bubble generator function is run, the reactor and column gasses are updated to reflect the bubble, the Column height calculator function is run, and a flag is set to indicate a bubble has occurred. The loop continues by checking the time against the column reset and sample times. If one of these occurs, the appropriate subroutine is entered, in which the column gas amounts and water height are updated to reflect the volume of gas removed with a syringe. The final step in the loop is to then use the collected raw data to calculate values, like gas volumes, for comparison to the physical experiment data, and write all data to the output file.

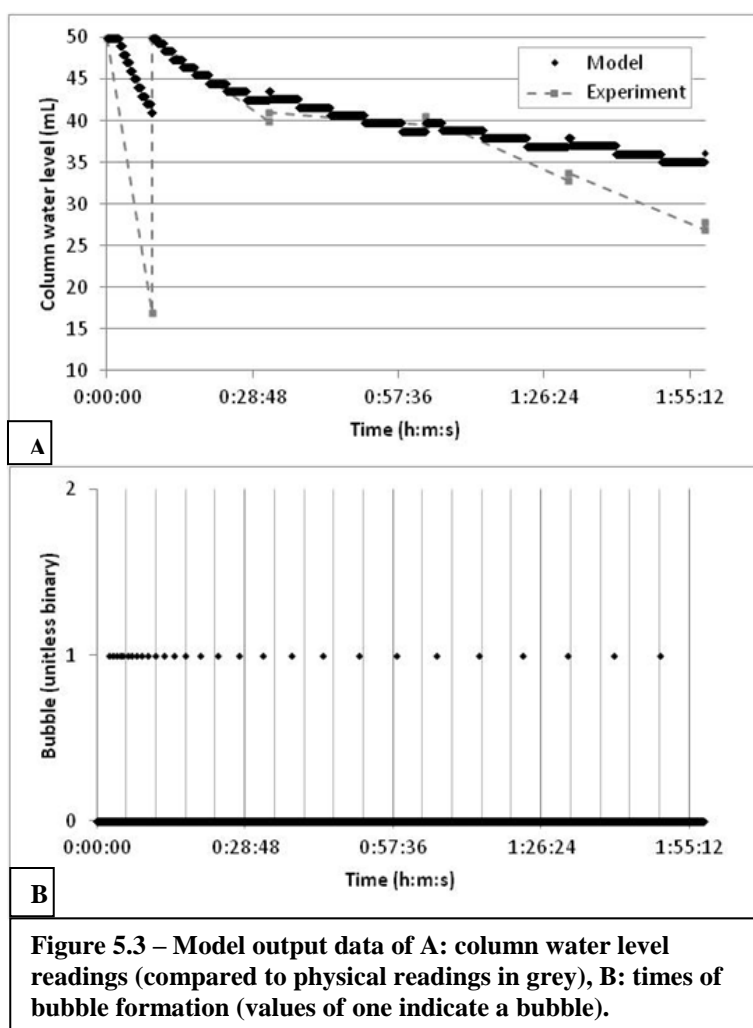
The loop iterates at chosen time intervals for a defined amount of time, and output intervals can be set to occur on every iteration or only when “events” occur. Finally, a completion message is given, and the user is returned to the Main Menu.

5.7 Approximations

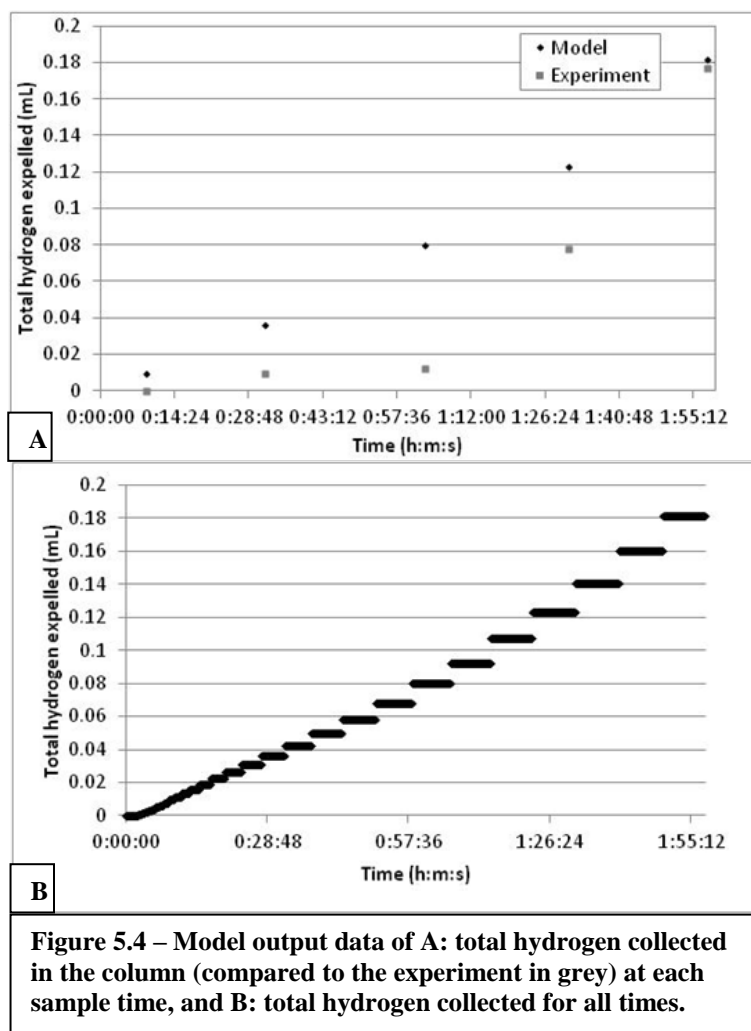
There are many assumptions about the mechanics that are made in the model, and some of them are clearly incorrect. Water vapor, for example is not ideal, but as mentioned above, this model is meant to be a simple approximation of the experiment. Development started with careful measurement of the physical properties of the reactor, and then the simplest zero order approximation of the process was created. This first model assumed constant hydrogen production rates, linear temperature profiles, and a total absence of water vapor and gas dissolution, among others. The results were not at all representative of the physical experiment, so the assumptions were examined and the temperature profile was changed to resemble the measurements taken. This process of testing, examining and refining repeated until the results began to converge on the expected trends. Meanwhile, experiments were run to isolate and test the influence of each of these variables. This approach provides insight into the hierarchy of influence of individual physical processes.

5.8 Model results

Many of the input parameters can be estimated or measured, and with optimization of the remaining parameters, the output resembles the results seen in the physical experiment. In the physical experiment, however, there are many limitations on the frequency, type, and location of measurements. This is due to a number of factors, including the manual recording, the 18min run time for each sample in the gas chromatograph, the necessity to keep the reactor sealed, and the standard difficulty in certain types of measurements. Because of this, by approximating the measurable results with the model, many of the extra variables in the output tells us what could be expected if measurements were taken without such limitations, i.e., measurement on short time scales and inside the reactor becomes virtually possible.

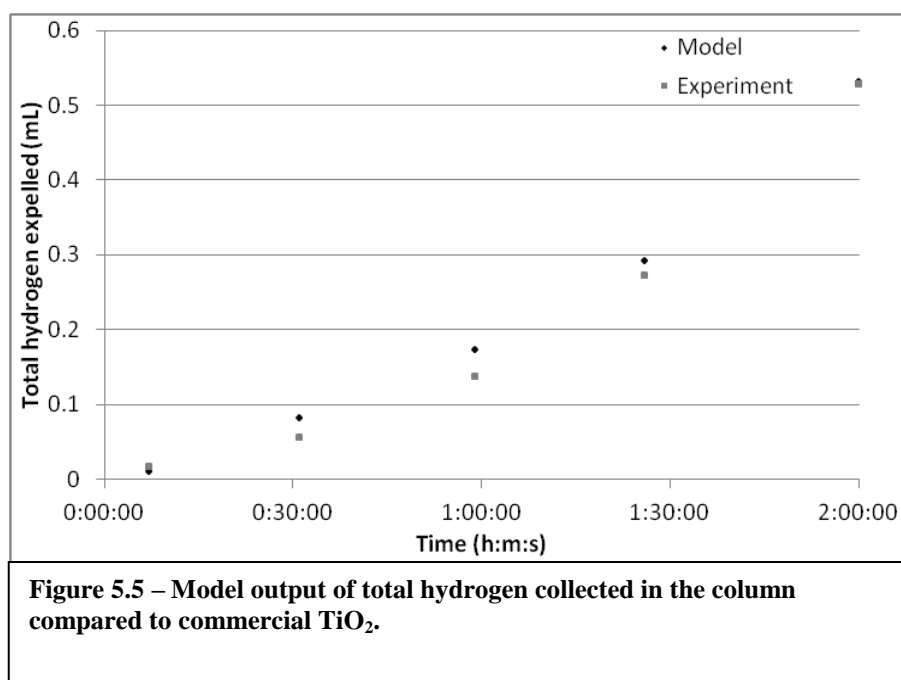


The model was run with the parameters set to replicate the 1%Fe-BTO experiment and results reported in the following chapter. Figures 5.3 and 5.4 show the output data that corresponds to the physical observations and measurements. Notice the output data is not the same as the reported physical results; specifically, the gas volume in the column is too



small, and too much hydrogen appears too early. The former is likely because the column gas is assumed to be dry. This assumption is certainly not accurate, but it only affects the total gas volume, not any of the hydrogen related properties, and the benefit of increased accuracy is outweighed by the considerable increase in complexity of the related volumetric calculations. The latter could be the result of a few neglected influences. First, spectral observations have revealed the emission spectrum and intensity changes drastically during the lamp's initial warm up period. It takes about two minutes for the mercury spectrum to stabilize and the intensity to reach a level similar to the steady state operation of the lamp. Second, the slurry and the column water are assumed to be totally

free of dissolved gasses and the argon and hydrogen are assumed to be completely insoluble. In actual measurements, however, carbon dioxide, nitrogen, and possibly oxygen are detected by the gas chromatograph; these gasses are likely released from solution as the temperature changes. Further, it has been shown that dissolved oxygen will form water with the addition of hydrogen in the presence of a catalyst or electrode^{20–22}. The BTO easily meets the energy requirement for this process, and it is likely this process is occurring to some extent, thereby reducing the hydrogen gas yield at early times.



On the other hand, figure 5.5 shows the model hydrogen result as compared to commercially produced TiO₂. In this graph, the model result follows the experimental result very closely. This suggests that while the attempts to explain the discrepancy above may still be true, there appears to be a fundamental difference between the behavior of the BTO and P25 at the reaction level. The discrepancy, in the hydrogen data, at least, cannot be ascribed to the mechanics of the reactor alone.

Despite the minor inconsistencies, these results are fairly close to the physical experiment; in figure 5.3, the general trend in (A) and the bubble pattern in (B) seem right on, while in figure 5.4, the curve in (A) does not match well, but the curve in figure 5.5 is much closer to the experimental data. More importantly, though, these results tell a more complete story. While the model shows a mere 0.18mL of hydrogen gas was collected in the column (and is thereby “measurable”) by the end of the 1% Fe-BTO experiment, a total of 9.1mL of hydrogen gas was produced, nearly 100 times the reported value, or 400 μ mol (compared to 6 μ mol in the column). Careful examination of figure 5.4 (B) shows a slight shoulder around 10-12min, which is not seen at all in the physical experiment. And finally, the model data in figure 5.3 (A) looks smooth, like an exponential growth more similar to the observed trend with the P25 samples than the BTO. It does not show the characteristic sudden change in slope, hinting that another process may be involved that deserves further investigation. Discussion of the importance of the new information provided by the model is given in the following chapter.

Chapter 6

Results

6.1 Hydrogen Experiment Results

The first step was to establish a baseline. The results of the experiment are compared to the standard set by titanium dioxide (TiO_2), specifically, Degussa P25, as it is a commercially produced product with significant quality controls, extensive characterization and is a consistent product. P25 (or at least some form of TiO_2) has appeared in many related works as either the test subject or the benchmark control. The P25 result from this experiment were compared to other works and found consistent with the published results^{3,4,23,24}.

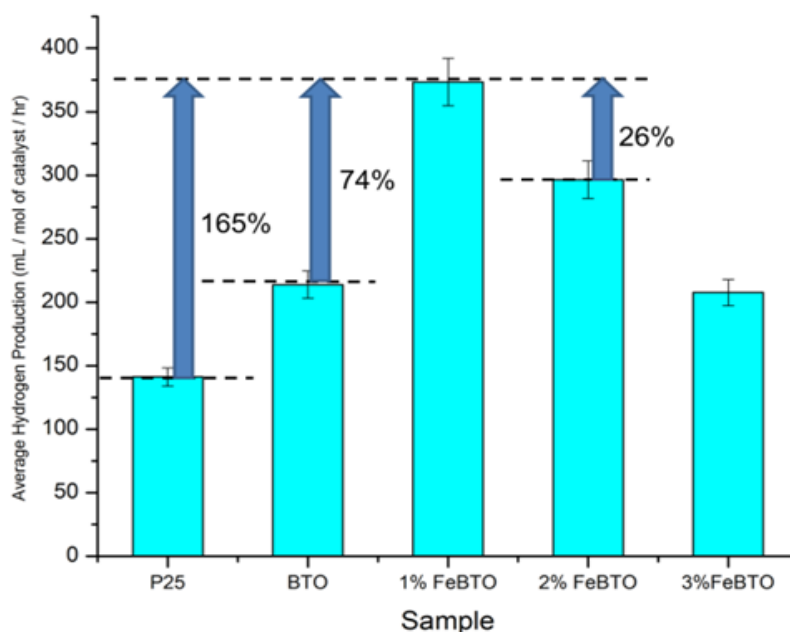


Figure 6.1 – Total H_2 yield over two hours for P25 and BTO samples with different iron substitution levels.

BTO with different iron inclusion ratios was compared in hydrogen gas production, as described in chapter 4, to P25, and it was found that pure BTO surpassed P25's performance, but the substitution with small amounts of iron for bismuth further improved the hydrogen production. Beyond 3% iron inclusion, the additional iron, besides manifesting increasingly as Fe_2O_3 , seemed to actually suppress the efficacy of the process.

As shown in figure 6.1, BTO produced 52% more hydrogen gas, in the experiment, than P25, but the real star is the BTO with 1% iron inclusion, which produced 74% more hydrogen than BTO, for a total 165% more hydrogen than P25, during the two hour exposure.

It is believed that the further iron substitution, which should improve the visible light absorbance by adding more impurity band sites, also may be shortening the electron-hole recombination rate or introducing defect sites on the crystal, which could account for the suppressed efficacy of the reaction.

It was found that all BTO samples from the pure (0%) to 3% iron inclusion were more effective than P25 in producing hydrogen gas in the experiment, but 1% FeBTO came out as a clear winner with a volume of hydrogen gas produced increase of 150% over P25, and a 74% and 26% increase over BTO and 2% BTO, respectively.

Interestingly, when the hydrogen produced is plotted as a function of time, seen in figure 6.2, an initially unexpected inflection point is apparent. This seems to possibly indicate a shift from a phase 1 dominated reaction to either a mixed or phase 2 dominated reaction as discussed in chapter 2. this shift happens for the different BTO samples at different times, with the 1% BTO sample happening earliest, which partially accounts for

the higher level of hydrogen gas production. This same shift is not seen in the results for the P25; a previous study shows this happening at around 8-10 hours in their reactor⁴.

When compared, side by side, the time resolved data show P25 producing more hydrogen gas than the BTO at early times, but after the shift, the faster rate of production in the BTO samples allows them to overtake the P25 at later times. If the shown trends continue a reasonable distance further in time, longer reaction periods would show an even larger increase in hydrogen production over P25.

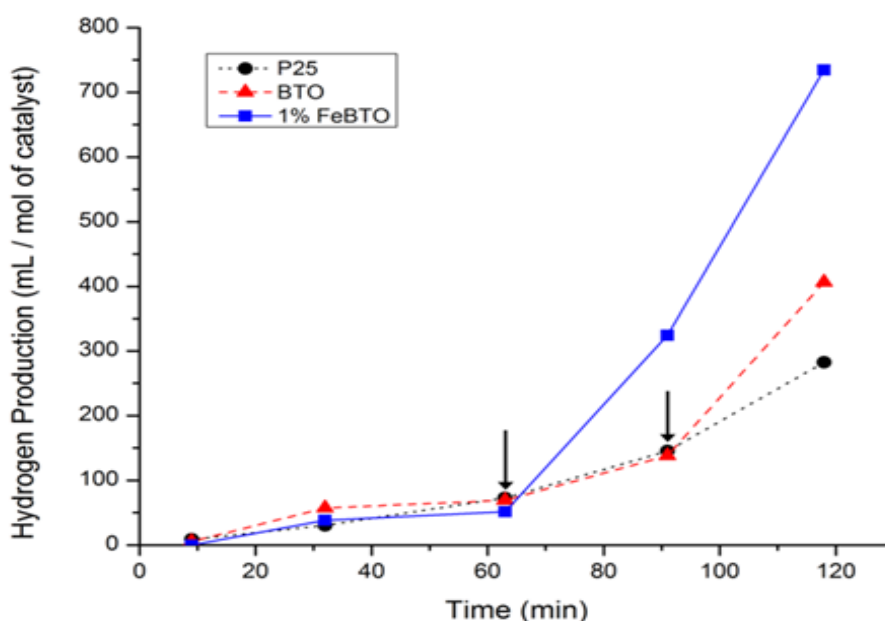


Figure 6.2 – Time resolved H₂ yield for P25, BTO, and 1% FeBTO. The arrows show inflection points in the generation rates of BTO and 1% FeBTO.

After multiple iterations of the same experiment, environmental conditions, primarily temperature and barometric pressure, were found to have an unacceptably large effect on the amount of hydrogen measured. For this reason, the data was collected in as short a period of time as possible (one to two days per set) in as close as possible to the same environmental conditions. The data presented is a representative set from a group of three similar sets collected over the course of a single week. Because of such variation, it

is important to restate that while my confidence in the absolute accuracy of the values reported is lower (estimated to be within about 10%), I am much more confident in the trends, the relative values in both the time-resolved and total hydrogen yield results.

6.2 Discussion

A simple and reliable method for synthesizing BTO was developed, and the product was characterized via various methods (chapter 2), all of which indicated we were synthesizing $\text{Bi}_2\text{Ti}_2\text{O}_7$ with the ability to substitute small amounts of Fe ions into the bismuth sites in the crystal. Chapter 3 provides the suspected processes which would allow a photocatalyst under illumination to free hydrogen gas from a mixture of water and methanol. The results of this experiment in chapter 4 empirically show a correlation between FeBTO and increased photocatalytic hydrogen gas generation. While many of the specifics of the reaction are not well known, because no control test could account for any other route, it is concluded that BTO is an effective material for this process, and low levels of iron inclusion greatly improve upon the pure BTO. In hydrogen experiments, BTO and FeBTO demonstrated an increased hydrogen yield over P25, as well as a stability and reusability rivaling that of P25. Interestingly, the increased hydrogen yield seems to be related to the timing of the inflection point shown in figure 6.2. It is suspected that the sudden change in generation rate is due to a transition from stage 1 to stage 2 as shown in figure 2.1.

The results of the model, discussed in chapter 5, using a standard Arrhenius rate equation, agreed well with the physical P25 results, which did not show the inflection point, but could not match the physical results of BTO or FeBTO, all samples of which

showed the inflection point at some time within the reaction period. This seems to indicate that there is indeed a shift in the hydrogen generation rate that cannot be accounted for by temperature or any of the other physical variables used in the model. Additionally, this seems to beg further investigation to determine the actual rate change and specific mechanism or mechanisms that dictate the behavior; it seems that if the rate change behavior can be exploited, the material can be even more greatly improved.

Further, to improve understanding of the reaction and allow development of dramatically improved photocatalysts, other aspects of the process need deeper investigation as well: the temperature dependence of the reaction seems very sensitive and should be characterized. Light intensity and wavelength studies, need to be made. Different dopants, pollutants, and mixture ratios, as well as stability properties all need to be investigated and characterized.

Much work has been done globally to develop a replacement for our current hydrocarbon economy. While this work has impacted the demand on hydrocarbons, no suitable replacement has yet emerged. One possible candidate is a hydrogen economy, but for that to become viable, an effective and efficient means, which is not hydrocarbon-dependent, to produce the fuel is necessary. Ideally, that process would also be part of a renewable cycle.

While photocatalytic hydrogen generation still cannot rival the output of electrolysis or steam reforming of natural gas, the work described above has made strides toward it being a viable option, enabling a renewable hydrogen economy. By using the abundant sunlight to harvest hydrogen from water and organic pollutants, photocatalytic hydrogen generation could help complete the supply side of the renewable energy cycle

in a hydrogen energy economy. Additionally, the use of industrial waste products in place of methanol as the organic sacrificial agent, water pollution could be mitigated.

References

- ¹ B. Allured, S. DelaCruz, T. Darling, M.N. Huda, and V. (Ravi) Subramanian, Appl. Catal. B Environ. **144**, 261 (2014).
- ² P.F. Bernath, *Spectra of Atoms and Molecules* (Oxford University Press, 1995).
- ³ H. Choi and M. Kang, Int. J. Hydrogen Energy **32**, 3841 (2007).
- ⁴ X. Yang, C. Salzmann, H. Shi, H. Wang, M.L.H. Green, and T. Xiao, J. Phys. Chem. A **112**, 10784 (2008).
- ⁵ J. Chen, D.F. Ollis, W.H. Rulkens, and H. Bruning, Water Res. **33**, 669 (1999).
- ⁶ R. Gao, J. Stark, D.W. Bahnemann, and J. Rabani, J. Photochem. Photobiol. A Chem. **148**, 387 (2002).
- ⁷ A. Nourmohammadi, R. Rahighi, O. Akhavan, and A. Moshfegh, J. Alloys Compd. **612**, 380 (2014).
- ⁸ S. Murugesan, M.N. Huda, Y. Yan, M.M. Al-Jassim, and V. (Ravi) Subramanian, J. Phys. Chem. C **114**, 10598 (2010).
- ⁹ S. Murugesan and V.R. Subramanian, Chem. Commun. (Camb). 5109 (2009).
- ¹⁰ Shimadzu Corporation, Fundamentals FTIR Anal. (2014).
- ¹¹ W.-D. Yang, Y.-H. Chang, and S.-H. Huang, J. Eur. Ceram. Soc. **25**, 3611 (2005).
- ¹² M. Mori and N.M. Sammes, **146**, 301 (2002).
- ¹³ R.G. Freitas, R.T.S. Oliveira, M.C. Santos, L.O.S. Bulhões, and E.C. Pereira, Mater. Lett. **60**, 1906 (2006).
- ¹⁴ J.H. Cai, G. Ni, G. He, and Z.Y. Wu, Phys. Lett. A **372**, 4104 (2008).
- ¹⁵ D.K. Smith and R. Jenkins, J. Res. Natl. Inst. Stand. Technol. **101**, 259 (1996).
- ¹⁶ Ace Glass, Lab. Glas. Sci. Equip. from Ace Glas. Inc. [Http://www.aceglass.com/contact.php](http://www.aceglass.com/contact.php) (2014).
- ¹⁷ SRI Instruments, GC, HPLC, Data Syst. Hydrog. Gener. [Http://www.srigc.com/](http://www.srigc.com/) (2014).

- ¹⁸ Evonik Degussa, AEROXIDE® P25- Evonik Ind. - Spec. Chem.
[Http://corporate.evonik.com/en/products/industry-Teams/solar-Power/products-applications/Pages/aeroxide.aspx](http://corporate.evonik.com/en/products/industry-Teams/solar-Power/products-applications/Pages/aeroxide.aspx) (2014).
- ¹⁹ P. Ahuja, *Chemical Engineering Thermodynamics* (PHI Learning Pvt. Ltd., New Delhi, 2009), p. 698.
- ²⁰ X. Tan and K. Li, *Chem. Eng. Sci.* **55**, 1213 (2000).
- ²¹ T. Ahmed and M.J. Semmens, *J. Memb. Sci.* **69**, 1 (1992).
- ²² S. Suppiah, K.J. Kutchcoskie, P. V. Balakrishnan, and K.T. Chuang, *Can. J. Chem. Eng.* **66**, 849 (1988).
- ²³ A. Sobczynski, *J. Mol. Catal.* **39**, 43 (1987).
- ²⁴ A. Sobczynski, T. Jakubowska, and S. Zielinski, *Monatshefte Für Chemie - Chem. Mon.* **120**, 101 (1989).